

pubs.acs.org/NanoLett Letter

Vertically Aligned Ag_xAu_{1-x} Alloyed Nanopillars Embedded in ZnO as Nanoengineered Low-Loss Hybrid Plasmonic Metamaterials

Robynne L. Paldi, Xuejing Wang, Xing Sun, Zihao He, Zhimin Qi, Xinghang Zhang, and Haiyan Wang*



Cite This: Nano Lett. 2020, 20, 3778-3785



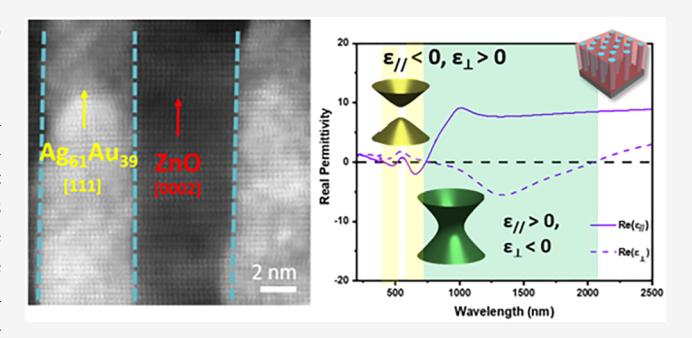
ACCESS

Metrics & More

Article Recommendations

3 Supporting Information

ABSTRACT: Hybrid plasmonic metamaterials offer a pathway to exotic properties and technologically important applications including subdiffraction imaging and plasmonic energy harvesting. Challenges remain for practical applications including high absorption losses of noble metals and tedious growth/fabrication processes. In this work, a self-assembled hybrid plasmonic metamaterial consisting of anisotropic Ag_xAu_{1-x} alloy nanopillars embedded in a ZnO matrix has been successfully grown. The chemical composition of the nanoalloy was determined to be Ag₆₁Au₃₉. The microstructure and optical properties arising from ZnO-Ag₆₁Au₃₉ alloyed hybrid systems were investigated and compared with that of the ZnO-Ag particle-in-matrix nano-



composite and the ZnO-Au vertically aligned nanocomposite. The $ZnO-Ag_{61}Au_{39}$ hybrid system demonstrates anisotropic morphology, excellent epitaxial quality, and enhanced optical properties, including surface plasmon resonance, hyperbolic dispersion, low absorption losses, and numerous epsilon-near-zero permittivity points, making it a promising candidate for practical applications of hybrid plasmonic metamaterials.

KEYWORDS: oxide-metal hybrid material, vertically aligned nanocomposite, nanoalloy, plasmonics, metamaterials

Hyperbolic metamaterials are a class of materials demonstrating unique dielectric function, owing to their anisotropic nanostructure. The anisotropic nanostructure leads to a hyperbolic dispersion in the dielectric function,, in which the dielectric function will behave as a metal in one direction and as a dielectric material in the opposite direction. Potential applications of hyperbolic metamaterials include subwavelength wave-guides, subdiffraction imaging, 2,3 cloaking,4 and platforms for studying fundamental physical phenomenom.^{5,6} The most popular approaches for realizing practical hyperbolic metamaterials are through layered dielectric-metal nanocomposites^{3,7,8} and nanowire arrays.^{9–12} Owing to the plasmonic coupling at the metal-dielectric heterointerface, nanostructured hyperbolic metamaterials have multifunctionalities not only as metamaterials, but also in energy harvesting and sensor technologies, 13-17 i.e. hybrid plasmonic metamaterials. Layered dielectric-metal nanocomposites have the advantage of being well-studied, but require top-down multistep depositions and are limited by materials selection.^{7,18} Conversely, nanowire arrays offer a promising bottom-up approach for realizing practical applications by the recently demonstrated oxide-metal vertically aligned nanocomposite (VAN) morphology. 19-21 Two-phase VAN thin films are functional materials consisting of nanopillars of one phase embedded in the matrix of the second phase, leading to unique multifunctionalities and highly anisotropic morphology and properties. 19,22-30 The VAN approach offers benefits over

top-down nanowire array growth methods, ^{31–34} including one-step self-assembly through the pulsed laser deposition (PLD) technique, robust materials selection, and extensive tailorable morphology.

One of the major limitations of metallic plasmonic metamaterials in practical applications is the high absorption losses of plasmonic noble metals such as Ag and Au. ^{14,19} Using nanostructured low-loss metals is proposed as one way to overcome absorption losses; some promising candidates include nanostructured aluminum^{35,36} and copper. ³⁷ While these metals are promising, they suffer from chemical and thermal instability issues. Another proposed but less studied way is utilizing nanoalloys. ^{38–41} Nanoalloys are a strong candidate for hybrid plasmonic metamaterials; however, they also suffer from chemical and thermal instability issues. ^{42,43} It could be possible to achieve a stable nanoalloy by combining it with a chemically stable oxide matrix.

In this work, we propose nanoscale alloying of the metallic constituent of oxide-metal VAN for a 2-fold effect. The first is

Received: February 22, 2020 Revised: April 4, 2020 Published: April 24, 2020





to create enhanced hybrid plasmonic metamaterials by utilizing nanoalloys for improved optical response and tunability 39,44 in oxide-metal VAN. Nanoalloys suffer from thermal stability issues in high temperatures, preventing them from advanced application. 42 Encapsulation in an oxide matrix will provide a platform for plasmonic hybridity and enhanced chemical and thermal stability. The second purpose of alloying the oxidemetal hybrid material is to enable VAN growth to overcome the typical particle-in-matrix oxide-metal form. Exotic functionalities of metamaterials depend on the strong anisotropy in the VAN nanostructures, while many of the oxide-metal hybrid materials prefer to grow as an isotropic particle-in-matrix structure, ^{21,45} limiting their anisotropic nature. By properly selecting the alloy composition with a metal preferring pillar structure, it is possible to facilitate the pillar-in-matrix growth for superior combined properties and microstructure.

For this demonstration, we have selected Ag_xAu_{1-x} alloyed nanopillars embedded in the ZnO matrix as a VAN through a single-step PLD technique, schematically shown in Figure 1.

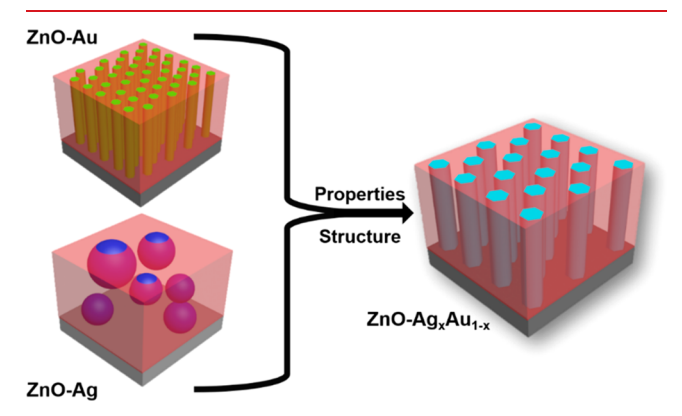


Figure 1. Schematic diagram of an oxide-alloyed metal vertically aligned nanocomposite. The alloy VAN approach enables the growth of the ZnO-Ag-type nanoalloy pillar-in matrix to produce a new metafilm with anisotropic morphology and broad optical properties.

Ag_xAu_{1-x} was chosen as the nanoalloy for this demonstration because of the widely studied plasmonic properties of Au and Ag. Ag has lower optical losses than Au; however, it is chemically unstable. Alloying Ag, together with Au, helps combine the optical properties of Ag with the chemical stability of Au. No. 2nO was selected as the dielectric medium as it is widely available and a well-studied photocatalytic and energy-harvesting material. As shown in Figure 1, ZnO-Ag and ZnO-Au were grown and compared to ZnO-Ag_xAu_{1-x}. ZnO-Ag has a preferred particle-in-matrix microstructure, while ZnO-Au grows as a pillar-in-matrix structure. Alloying Ag with Au in the ZnO matrix will grow ZnO-Ag_xAu_{1-x} with a vertical, anisotropic microstructure as seen in Figure 1. The microstructures of ZnO-Ag, ZnO-Au, and ZnO-Ag_xAu_{1-x} were carefully investigated and compared. The optical properties were measured and compared with single metal cases to demonstrate the structure and property tunability.

Results/Discussion. The challenge of alloying at the nanoscale was overcome by selecting compatible alloy constituents that were immiscible in the ZnO matrix. For comparison, ZnO-Ag and ZnO-Au hybrid materials were grown at the same parameters as ZnO-Ag_xAu_{1-x} on the α -Al₂O₃ [0001] substrate (see Methods section). The chemical composition of the nanoalloy was determined through energy

dispersive spectroscopy (EDS) and found to be Ag₆₁Au₃₉; the resulting table can be found in Table S1. The ZnO-Ag particlein-matrix can be seen in the cross-sectional scanning transmission electron microscopy (STEM) image in Figure 2a and plan-view in Figure 2d. Depicted in STEM images, the morphology of ZnO-Ag is particle-in-matrix. The inset SAED pattern in Figure 2a shows the low epitaxial quality of the ZnO-Ag particle-in-matrix nanocomposite. There are satellite diffraction peaks, caused by minor orientations of Ag and ZnO. Figure 2b shows vertical and well-ordered Au nanopillars inside a ZnO matrix. Plan-view STEM in Figure 2e shows individual Au nanopillars with a hexagonal shape and mesoscale quasi-hexagonal in-plane ordering. The inset image shows the SAED pattern, with diffraction spots from Au, ZnO, and Al₂O₃, indicating the high epitaxial quality. The out-ofplane epitaxial relationship is Al₂O₃ (0006) || ZnO (0002) || Au (111), and the in-plane relationship is Al_2O_3 (11 $\overline{2}0$) || ZnO $(10\overline{10})$ || Au $(2\overline{20})$. High epitaxial quality, like in ZnO-Au, is preferred as it leads to enhanced optical properties.⁴⁷ EDS chemical mapping of ZnO-Au and ZnO-Ag can be found in Figure S1, showing no interdiffusion between phases. Successful oxide-nanoalloy ZnO-Ag₆₁Au₃₉VAN growth is presented in Figure 2c,f. The cross-sectional STEM indicates vertical growth of the alloyed phase, while the inset SAED pattern shows the high epitaxial quality and the same out-ofplane and in-plane epitaxial relationship maintained from the ZnO-Au nanocomposite. Comparing microstructures indicates that alloying is an effective approach to induce pillar-in-matrix morphology for materials like Ag that grow with preferred particle-in-matrix morphology. X-ray diffraction (XRD) scans of the films and their targets were performed to investigate the microstructure and epitaxial quality, and a discussion can be found in Figure S2. Furthermore, it is possible to tune the alloy composition by varying the target stoichiometry or growth parameters. For demonstration, the background pressure was tuned, and besides the Ag₆₁Au₃₉ nanoalloy deposited at 20 mTorr, two other compositions of Ag₃₃Au₆₇ and Ag₆₇Au₃₃ were determined for deposition in a vacuum and 150 mTorr, respectively. The graph of the Ag/Au ratio vs deposition pressure of these films can be seen in Figure S3a, which was calculated based on the EDS data summarized in Table S1-3. A ratio of Ag/Au < 1 implies that the alloy is Au-rich, while a ratio of Ag/Au > 1 implies that the alloy is Ag-rich.

The alloyed growth in Figure 2c has a few interesting microstructural characteristics compared to the vertical ZnO-Au growth. The major difference when comparing ZnO-Au and ZnO-Ag61Au39 is apparent in the plan-view image. The alloyed pillars of ZnO-Ag₆₁Au₃₉ maintained a similar hexagonal shape and quasi-hexagonal ordering; however, nanoalloy pillars were larger than Au pillars in the ZnO-Au nanocomposite. The average diameters of the ZnO-Au and ZnO-Ag₆₁Au₃₉ pillars were calculated, and the distribution of pillar diameter was plotted in Figure S4. Diameter calculations were conducted by measuring the diameter of nanopillars via 3DS micrograph software in plan-view images in Figure 2 and plotting them as a histogram in Figure S4. This method is adopted from the calculation of particle size distributions.⁵⁰ ZnO-Au pillars have an average diameter of 6.14 nm, while ZnO-Ag₆₁Au₃₉ pillars have an average diameter of 13.7 nm. The diameter for the ZnO-Ag was not calculated due to irregular morphology. Comparing the growth of the alloy film to that of the ZnO-Au film indicates Ag has an increased pillar diameter. Moreover, some particles appear in the alloy film, most likely influenced

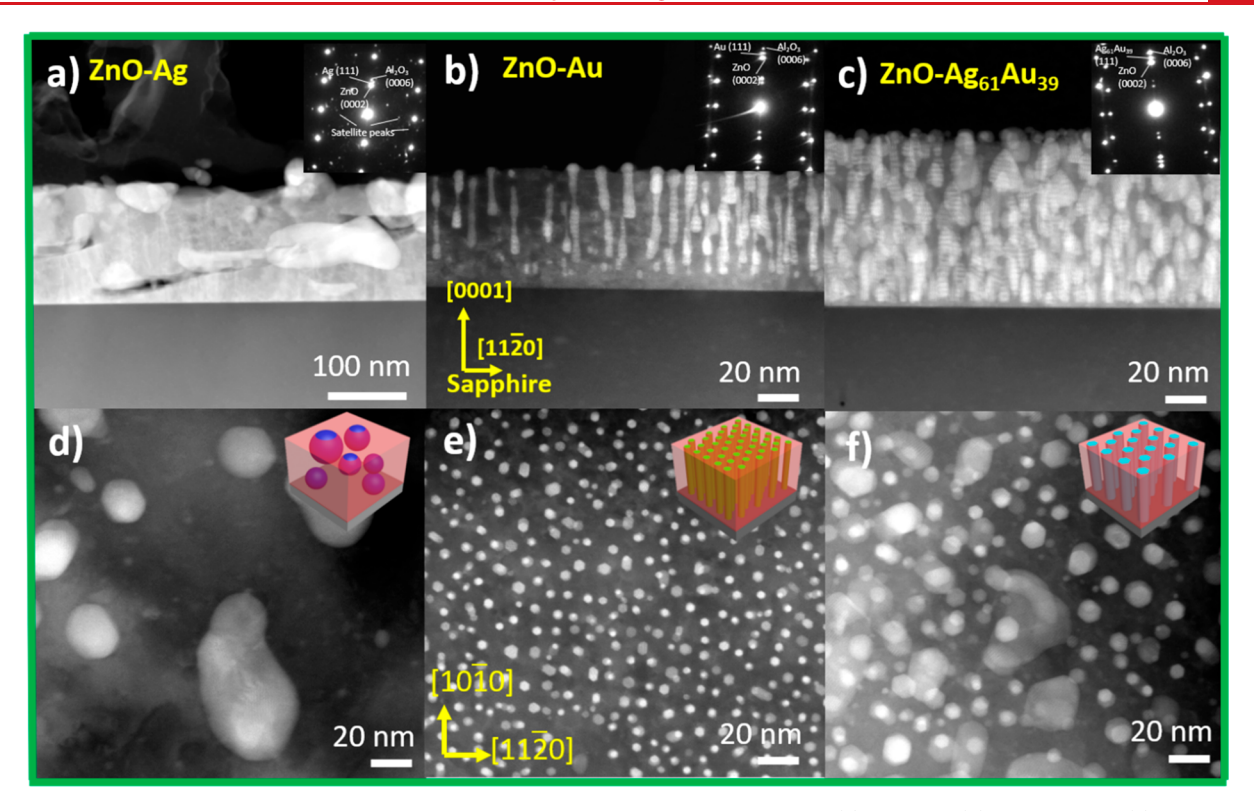


Figure 2. Comparison study of ZnO-Ag, ZnO-Au, and ZnO-Ag $_{61}$ Au $_{39}$. Cross-section images of (a) ZnO-Ag, (b) ZnO-Au, and (c) ZnO-Ag $_{61}$ Au $_{39}$. Insets are the corresponding SAED patterns. The bottom row of plan-view images corresponds to (d) ZnO-Ag, (e) ZnO-Au, and (f) ZnO-Ag $_{61}$ Au $_{39}$. Inset are models of corresponding films.

by Ag. Ag tends to have intraplanar diffusion, leading to large particle growth as seen in the ZnO-Ag sample in this work or even leads to tilted pillar growth in other VAN. It is possible to tune the morphology of ZnO-Ag, Au_{1-x} to make the pillars more uniform in the matrix, similar to the ZnO-Au growth. This was achieved by tailoring the growth parameters and performing the deposition under vacuum. The new optimized morphology can be seen in the TEM cross-sectional micrograph in Figure S3b, where pillars are uniformly distributed in the matrix. Moreover, the TEM plan-view image in Figure S3c depicts well-ordered pillar distribution.

A detailed microstructure characterization study was performed on the ZnO-Ag₆₁Au₃₉ VAN and presented in Figure 3. Figure 3a shows a high-resolution plan-view transmission electron micrograph (HRTEM), indicating the hexagonal shape of nanopillars and the (111) in-plane stacking arrangement. The sides of nanopillars are of {220} planes. Figure 3b presents a STEM plan-view image, showing the quasi-hexagonal ordering maintained from the ZnO-Au microstructure. The EDS maps, coupled with STEM images, shown in Figure 3c-f, depict the chemical composition of the nanoalloy VAN. Figure 3c shows a composite of all measured maps with no overlap between the alloy or ZnO, indicating phase separation between the matrix and nanopillars. Figure 3d,f presents the EDS map of Ag and Au, respectively. From the plan-view EDS map, the Au and Ag signals appear evenly mixed, indicating no significant phase separation in the nanopillars and that the nanopillars are well alloyed. Figure 3k shows a cross-sectional STEM image with the corresponding EDS elemental mapping shown in Figure 3g-j. The maps for Ag and Au appear in Figure 3h,j, respectively, and confirm that there is no phase separation and interdiffusion to the

matrix in the alloy, as seen in the plan-view EDS maps. Figure 3g is a composite of the measured maps and, like the plan-view EDS, indicates no overlap between the nanopillars and the oxide matrix. High-resolution STEM was performed on the cross-section sample in Figure 3l to discern the atomic structure and stacking arrangement. The alloy nanopillars grow with out-of-plane [111] direction and have an FCC stacking sequence. The growth direction of nanopillars matches with the HCP atomic stacking of ZnO and [0002] out-of-plane growth direction.

The optical properties of ZnO-Ag₆₁Au₃₉, ZnO-Ag, and ZnO-Au were compared using UV-vis spectroscopy as shown in Figure 4. Images of the bulk thin films are shown in Figure 4a, where ZnO-Ag has a film color of dark gray, and ZnO-Au has a red-blue appearance; ZnO-Ag₆₁Au₃₉ is a deep-scarlet red color. The physical appearance of plasmonic films depends on different factors including particle size, composition, and density. 52 Bimetallic alloys of Ag_xAu_{1-x} have been predicted to hybridize their plasmonic resonance and produce a deep, scarlet red color,³⁵ similar to the color observed in the ZnO-Ag₆₁Au₃₉ VAN. UV-vis spectroscopy was performed on each film to measure the transmission and plasmonic resonance; the resulting responses are presented in Figure 4b. ZnO-Au has a plasmonic resonance around 565 nm, ZnO-Ag has a resonance at 504 nm, and ZnO-Ag₆₁Au₃₉ has a resonance at 512 nm. The observed SPR of ZnO-Ag_xAu_{1-x} falls within the range predicted of the effective medium theory for Ag_xAu_{1-x} nanoalloys.³⁵ The plasmonic properties coupled with chemical and thermal stability of ZnO makes the ZnO-Ag $_{61}$ Au $_{39}$ VAN a potential candidate for applications in chemical sensing, biosensing,³¹ and energy harvesting.^{15,53}

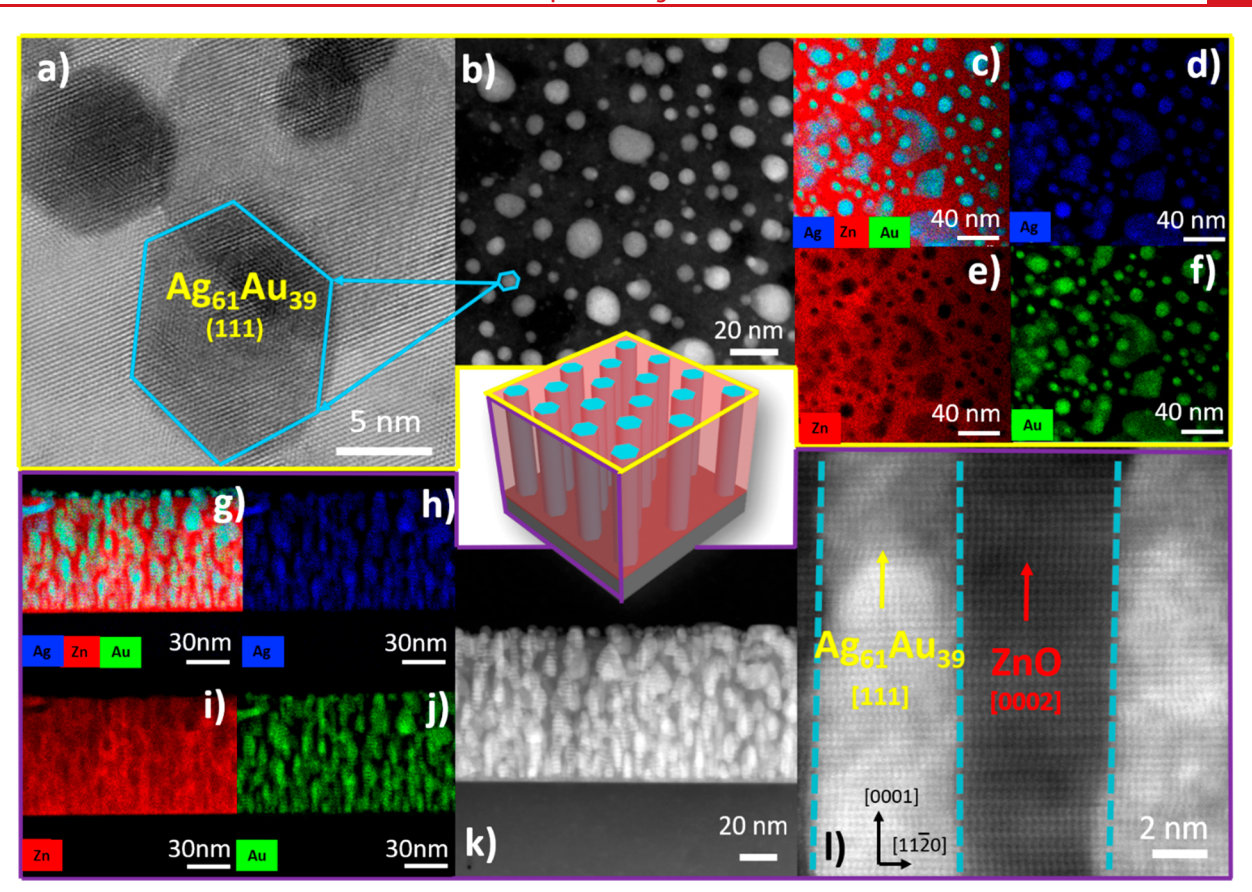


Figure 3. Detailed microstructural characterization of ZnO-Ag $_{61}$ Au $_{39}$. At the center is a model of VAN; the images are outlined in yellow and correspond to plan-view and are of the (a) HRTEM plan-view image of individual nanopillars. (b) STEM image showing plan-view morphology. EDS chemical mapping is shown in the (c) combined map, (d) Ag map, (e) Zn map, and (f) Au map. The bottom row outlined in purple related to cross-section and EDS mapping shows the (g) combined map, (h) Ag map, (i) Zn map, and (j) Au map. (k) STEM cross-section image showing VAN morphology. (l) HRSTEM cross-section showing atomic stacking.

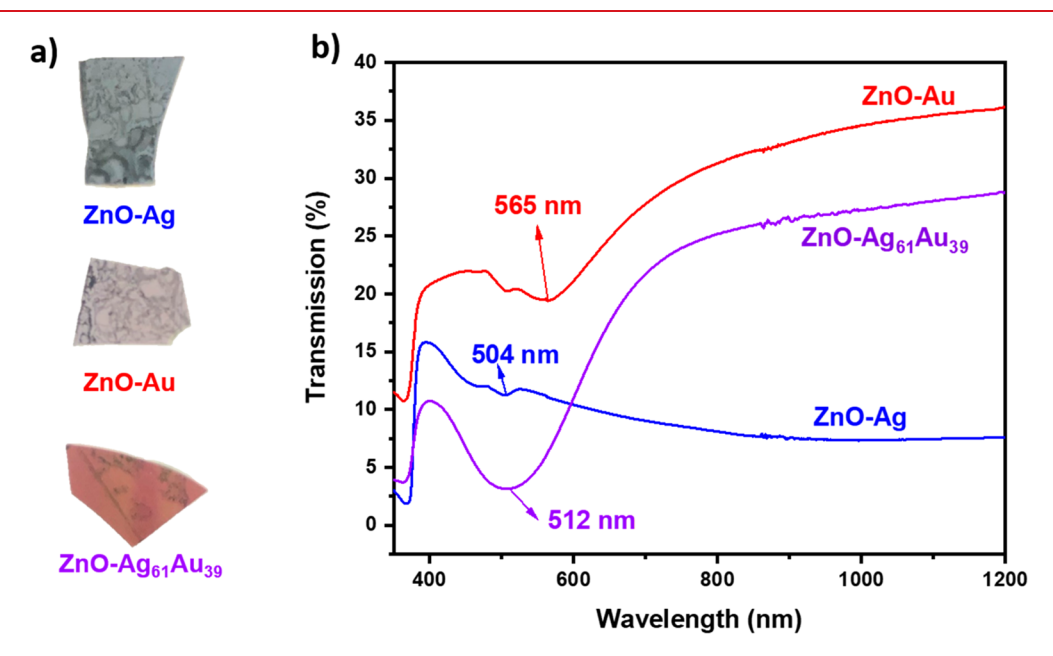


Figure 4. Transmission. (a) Images of bulk films presented. (b) The measured transmission from UV-vis spectroscopy.

The anisotropic microstructure of the oxide-metal VAN can be used to engineer a hyperbolic dispersion. ¹⁹ To investigate the anisotropic dielectric function of the ZnO-Ag₆₁Au₃₉ VAN, spectroscopic ellipsometry was performed from 210 to 2500

nm to measure the dielectric permittivity as shown in Figure 5. The perpendicular and parallel components of permittivity were resolved by using a uniaxial model coupled with the B-spline model. The measured ellipsometry data and fitted

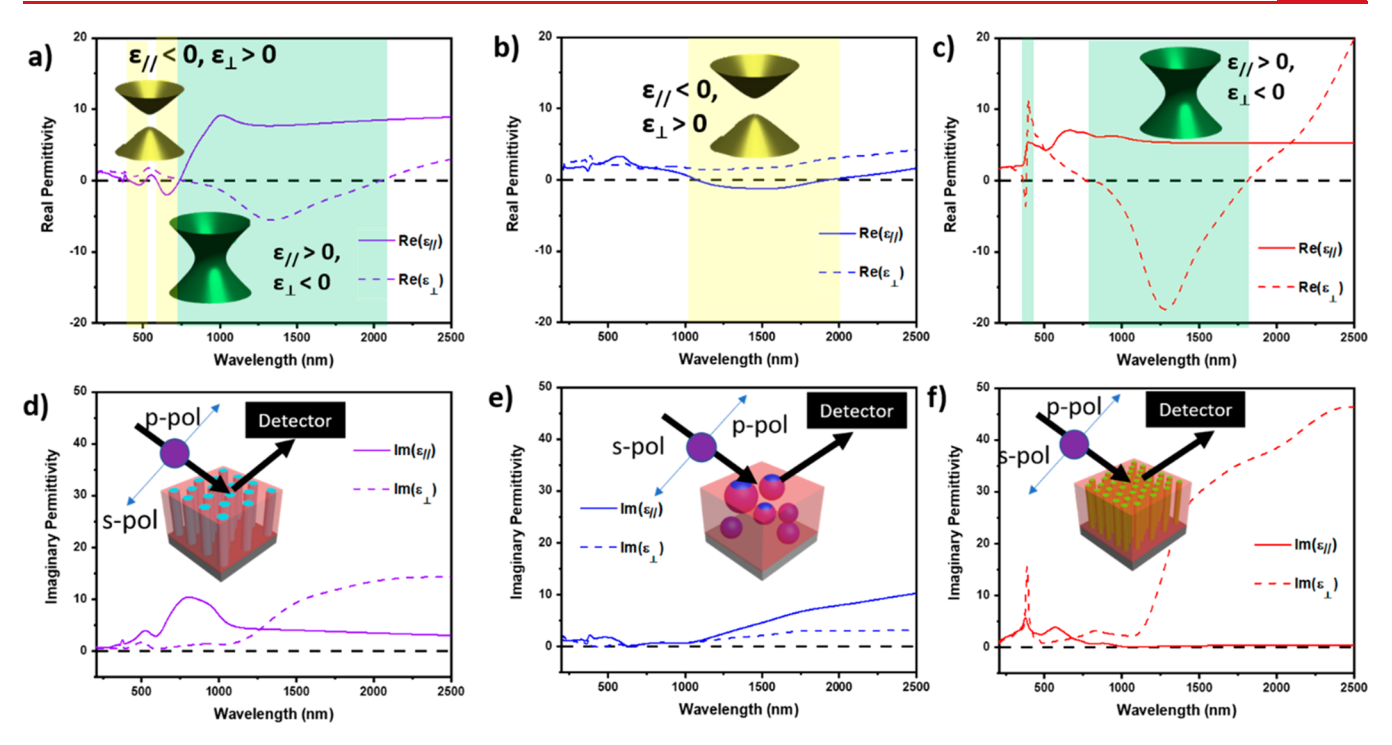


Figure 5. Dielectric function. The real part of permittivity for (a) ZnO- Ag_xAu_{1-x} , (b) ZnO-Ag, and (c) ZnO-Au. Imaginary permittivity of (d) ZnO- $Ag_{61}Au_{39}$, (e) ZnO-Ag, and (f) ZnO-Au. Insets in panels a—c are representative the isofrequency curve for type I hyperbolic metamaterial (yellow regime) and type II hyperbolic metamaterial (green regime). Insets in panels c and d are the experimental setup for ellipsometry measurement for respective nanocomposite thin film.

models for Ψ and Δ of each film can be found in Figure S5. Moreover, the dielectric response of the alloy VAN was compared with ZnO-Ag and ZnO-Au. The experimental setup with respect to the microstructure is inset in Figure 5d-f. The real parts of ZnO-Ag₆₁Au₃₉, ZnO-Ag, and ZnO-Au are plotted in Figure 5a-c, respectively, while the imaginary parts are plotted in Figure 5d-f, respectively. Hyperbolic regimes are highlighted on the real permittivity graph color-coded to the type of hyperbolic metamaterial, indicating their photonic density of k-states and isofrequency curve. Type I ($\varepsilon_{//} > 0$, ε_{\perp} < 0) hyperbolic regimes are highlighted with yellow, and type II $(\varepsilon_{//} < 0, \varepsilon_{\perp} > 0)$ hyperbolic regimes are highlighted green. The isofrequency curve of type I hyperbolic metamaterial can be described as a hyperboloid of two sheets, indicating support of high and low k-states. The isofrequency curve of type II hyperbolic metamaterial can be described as a paraboloid of one sheet and supports only high k-states.8 To confirm the surface plasmon resonance calculated from the UV-vis transmission spectra, angular reflectivity measurements were also performed on the ellipsometer and presented in Figure S6 at angles of 40°, 50°, 60°, and 70°. To confirm the validity of the model used to derive the complex dielectric function, the same uniaxial B-spline model was fitted to the measured angular reflectivity. The measured reflectivity demonstrated SPR at 520 nm for ZnO-Ag₆₁Au₃₉, 500 nm for ZnO-Ag, and 610 nm for ZnO-Au. Simulated reflectivity models demonstrated SPR within ~20 nm, confirming a good agreement between the simulation and experimental results.

The real and imaginary parts of dielectric permittivity of ZnO-Ag₆₁Au₃₉ VAN are plotted in Figure 5a,d, respectively. ZnO-Ag real and imaginary permittivity are depicted in Figure 5b,e, respectively, while the data of ZnO-Au are presented in Figure 5c,f, respectively. Anisotropy of the VAN microstructure is obvious when comparing $\varepsilon_{//}$ and ε_{\perp} components

for ZnO-Au and ZnO-Ag₆₁Au₃₉. The more isotropic particlein-matrix microstructure of ZnO-Ag is evident in $\varepsilon_{//}$ and ε_{\perp} components having a similar plot, minor differences due to irregular particle shape as seen in plan-view in Figure 2d. The ZnO-Ag₆₁Au₃₉ out-of-plane (ε_{\perp}) component has epsilon-nearzero (ENZ) permittivity at 736 and 2060 nm, while the inplane $(\varepsilon_{//})$ component has ENZ permittivity at 400, 520, 590, and 736 nm. Moreover, ZnO-Ag61Au39 hybrid material demonstrates three hyperbolic regimes: type 1 hyperbolic regimes occur from 400 to 520 nm and 590-736 nm, and a type II hyperbolic region occurs from 736 to 2050 nm. Interestingly, ZnO-Ag has a hyperbolic regime ranging from 1000-2100 nm with ENZ permittivity occurring at 1000 and 2100 nm. ZnO-Au has a hyperbolic regime from 362 to 382 nm and 758–1820 nm with ENZ permittivity occurring at 362, 382, 758, and 1820 nm in the ε_{\perp} component. Both ZnO-Ag and ZnO-Au have a similar hyperbolic regime in the nearinfrared occurring from 1000 to 2100 nm for ZnO-Ag and 758-1820 nm for ZnO-Au, but ZnO-Ag is a type I hyperbolic metamaterial, while ZnO-Au is a type II hyperbolic metamaterial. ZnO-Ag₆₁Au₃₉ has inherited the hyperbolic properties of ZnO-Au in this regime and has a type II hyperbolic regime from 736 to 2050 nm. ZnO-Au demonstrates high absorption losses in its near-infrared hyperbolic regime (758-1820 nm), depicted in Figure 5e. This is in contrast with the imaginary permittivity of ZnO-Ag in Figure 5f, which has overall much lower values in the near-infrared hyperbolic regime. By alloying Ag and Au, ZnO-Ag₆₁Au₃₉ VAN has maintained similar hyperbolic regimes in near-infrared as ZnO-Au and has much lower values of imaginary permittivity as seen in Figure 5f. While ZnO-Ag does demonstrate a hyperbolic regime in the near-infrared, it does not have visible regime hyperbolic regimes. Alloying in the ZnO-Ag₆₁Au₃₉ hybrid material has improved and rectified the shortcomings

of both ZnO-Au and ZnO-Ag nanocomposites. ZnO-Ag₆₁Au₃₉ has lower absorption losses than ZnO-Au and demonstrates hyperbolicity in the visible regime, where ZnO-Ag is lacking. All of these, coupled together, indicate that alloying is an effective approach for tuning optical functionality. Moreover, the ZnO-Ag₆₁Au₃₉ VAN has demonstrated more significant hyperbolic dispersion and ENZ permittivity across a broad range of wavelengths with low associated imaginary permittivity as compared with other Ag/Au nanowire hyperbolic metamaterial in both the near-infrared and visible regimes. 8,9,19,54-58 Through the unique one-step self-assembly alloy approach in this report, it is possible to grow pillar-inmatrix ZnO-Ag type hyperbolic metamaterials, where ZnO-Ag usually prefers particle-in-matrix morphology due to complex growth conditions. Furthermore, this approach allows for thin film integration across various substrates and surfaces, broadly expanding the application of HMM and nanoalloys.

Oxide-alloyed metal-based VANs open an entirely new paradigm of multifunctionality, as it combines the field of nanoalloys with the VAN platform. The ZnO-Ag₆₁Au₃₉ film demonstrated a broad range of hyperbolic properties and SPR when compared with other Ag/Au nanowire arrays. Therefore, the ZnO-Ag₆₁Au₃₉ VAN is envisioned as an ideal candidate for multifunctional applications in both the fields of hyperbolic metamaterials and plasmonics, specifically in the application of subdiffraction imaging and far-field hyperlenses. 8,13 The optical losses and properties in this work could be further engineered by varying the alloy composition and incorporating other metals in alloy form, such as the inclusion of other low-loss metals like Cu or Al. As seen from the preliminary data in Figure S7, it is possible to achieve ZnO-Au_xCu_{1-x} with nanopillar morphology and well-ordered in-plane structure based on the cross-section and plan-view STEM and EDS mapping results. The investigation on the effect of Cu alloying with Au in the ZnO dielectric matrix on optical properties is currently ongoing. Further improvements could be achieved by alloying with other optically interesting metals, and exotic functionalities could be realized through incorporating magnetic alloy compositions, such as Fe, Co, and Ni.

In conclusion, this work presents a new oxide-metallic alloybased VAN consisting of ZnO and Ag₆₁Au₃₉ alloy nanopillars. ZnO-Ag₆₁Au₃₉ was deposited through a one-step pulsed laser deposition method and compared with that of the single-case ZnO-Ag and ZnO-Au nanocomposite. Microstructural characterization shows that the new alloyed VAN inherits the epitaxy and anisotropy of the ZnO-Au VAN. Spectroscopic ellipsometry was performed to investigate the anisotropic dielectric response of ZnO-Ag₆₁Au₃₉ and compared to ZnO-Au and ZnO-Ag. The alloyed VAN has demonstrated interesting hyperbolic dispersion and ENZ permittivity as compared with anisotropic ZnO-Au and other Ag/Au nanowire array hyperbolic metamaterials. UV-vis spectroscopy measurements discerned the plasmon response of all films. Angular reflectivity measurements were conducted to confirm the plasmon resonance and compare the response of the alloy VAN to that of ZnO-Ag and ZnO-Au. The ZnO-Ag61Au39 alloy film possesses broad optical properties for metamaterial application, indicating the potential of alloyed nanopillars in the field of nanophotonics to produce multifunctional hybrid plasmonic metamaterials. The alloyed oxide-metal hybrid materials also demonstrated a new route for property tuning in nanoscale metamaterial designs. Future work includes the investigation

and systematic study of other alloy candidates toward a broad range of morphology and property tuning.

Methods. For thin-film growth, ZnO-Au, ZnO-Ag, and ZnO-Ag₆₁Au₃₉ nanocomposite films were grown on c-cut Al₂O₃ (0001). The deposition was performed with a KrF excimer laser (Lambda Physik Complex Pro 205, $\lambda = 248$ nm), and the substrate temperature was kept constant at 500 °C. The laser beam was focused with an incident angle of 45° with laser energy of 420 mJ. The target-substrate distance was kept constant at 4.5 cm and measured before each deposition to ensure accuracy. Three nanocomposite targets consisting of ZnO-Ag, ZnO-Au, and ZnO-Ag₅₀Au₅₀were developed through solid-state sintering used for laser ablation. Before deposition, the chamber was pumped down to around 10-6 mTorr before an oxygen pressure was inflowed. The oxygen background pressure was maintained at 20 mTorr, and the laser pulse frequency was set to 5 Hz for all depositions. After all depositions, the chamber was cooled to room temperature at a rate of 15 °C/min.

Microstructure Characterization. Film morphology was characterized through XRD, TEM, and STEM coupled with EDS mapping. XRD scans of θ –2 θ were conducted using a Panalytical X'Pert X-ray diffractometer with Cu K α radiation. Bright-field TEM, STEM, SAED patterns, and EDS mapping were performed in an FEI Talos F200X TEM. Samples for electron microscopy were prepared, for both cross-section and plan-view, via a standard grinding procedure, which entails manual grinding, polishing, dimpling, and a final ion milling step to achieve electron transparency (PIPS 691 precision ion polishing system, 5 keV for cross-section and 4–4.5 keV for plane-view sample).

Optical Measurements. Ellipsometry experiments were carried out on an RC2 Spectroscopic ellipsometer (J.A. Woollam Company). Three angles, 30°, 45°, and 60°, were measured from a spectrum range of 210–2500 nm. Ψ and Δ data were obtained from ellipsometry experiments and then fit with a uniaxial model coupled with a B-spline model that was used to discern anisotropic permittivity properties of ZnO-Au, ZnO-Au, and ZnO-Ag₆₁Au₃₉; an agreeable mean square error (MSE) < 5 was obtained for all film models. Angular reflectivity measurements were performed on an RC2 Spectroscopic ellipsometer at 40°, 50°, 60°, and 70° and fitted with a uniaxial B-spline model to confirm surface plasmon resonance. Normal incident depolarized transmittance (T%) was measured using an optical spectrophotometer (Lambda 1050 UV—vis spectrophotometer).

ASSOCIATED CONTENT

5 Supporting Information

The Supporting Information is available free of charge at https://pubs.acs.org/doi/10.1021/acs.nanolett.0c00790.

EDS mapping of ZnO-Au and ZnO-Ag, XRD pattern for all films, composition and morphology tuning of ZnO-Ag, Au_{1-x} oxide-nanoalloy thin films, diameter calculation, ellipsometry measured and model data for Ψ and Δ , measured and model angular reflectivity, and microstructural characterization of the ZnO-Au, Cu_{1-x} VAN thin film (PDF)

AUTHOR INFORMATION

Corresponding Author

Haiyan Wang — School of Materials Engineering and School of Electrical and Computer Engineering, Purdue University, West Lafayette, Indiana 47907, United States; orcid.org/0000-0002-7397-1209; Email: hwang00@purdue.edu

Authors

Robynne L. Paldi – School of Materials Engineering, Purdue University, West Lafayette, Indiana 47907, United States

Xuejing Wang – School of Materials Engineering, Purdue University, West Lafayette, Indiana 47907, United States

Xing Sun – School of Materials Engineering, Purdue University, West Lafayette, Indiana 47907, United States

Zihao He — School of Electrical and Computer Engineering, Purdue University, West Lafayette, Indiana 47907, United States

Zhimin Qi – School of Materials Engineering, Purdue University, West Lafayette, Indiana 47907, United States

Xinghang Zhang – School of Materials Engineering, Purdue University, West Lafayette, Indiana 47907, United States

Complete contact information is available at: https://pubs.acs.org/10.1021/acs.nanolett.0c00790

Author Contributions

The project was conceived and led by H.W. R.L.P. deposited the films and conducted the property measurements. R.L.P. conducted optical measurement and analysis. X.S, X.W, Z.H., and R.L.P. prepared the TEM samples and conducted the TEM study. The manuscript was drafted and revised by R.L.P., H.W., and X.Z., and all authors have revised and given the approval for the final version of the manuscript.

Notes

The authors declare no competing financial interest.

ACKNOWLEDGMENTS

This work was supported by the U.S. Department of Energy, Office of Science, Basic Energy Sciences under Award DE-SC0020077. R.L.P. acknowledges the funding support from the Purdue Doctoral Fellow program and Sandia National Lab LDRD Diversity Fellow program. X.S. and X.W. acknowledge the support from the U.S. National Science Foundation (DMR-1565822) for the high-resolution TEM/STEM characterization effort.

REFERENCES

- (1) He, Y.; He, S.; Yang, X. Optical Field Enhancement in Nanoscale Slot Waveguides of Hyperbolic Metamaterials. *Opt. Lett.* **2012**, *37* (14), 2907–2909.
- (2) Jacob, Z.; Alekseyev, L. V.; Narimanov, E. Optical Hyperlens: Far-Field Imaging beyond the Diffraction Limit. *Opt. Express* **2006**, *14* (18), 8247.
- (3) Wood, B.; Pendry, J. B.; Tsai, D. P. Directed Subwavelength Imaging Using a Layered Metal-Dielectric System. *Phys. Rev. B: Condens. Matter Mater. Phys.* **2006**, 74 (11), 1–8.
- (4) Tumkur, T. U.; Kitur, J. K.; Chu, B.; Gu, L.; Podolskiy, V. A.; Narimanov, E. E.; Noginov, M. A. Control of Reflectance and Transmittance in Scattering and Curvilinear Hyperbolic Metamaterials. *Appl. Phys. Lett.* **2012**, *101* (9), 091105.
- (5) Smolyaninov, I. I.; Hwang, E.; Narimanov, E. Hyperbolic Metamaterial Interfaces: Hawking Radiation from Rindler Horizons and Spacetime Signature Transitions. *Phys. Rev. B: Condens. Matter Mater. Phys.* **2012**, *85* (23), 1–7.

- (6) Smolyaninov, I. I. Analog of Gravitational Force in Hyperbolic Metamaterials. *Phys. Rev. A: At., Mol., Opt. Phys.* **2013**, 88 (3), 1–4.
- (7) Maas, R.; Parsons, J.; Engheta, N.; Polman, A. Experimental Realization of an Epsilon-near-Zero Metamaterial at Visible Wavelengths. *Nat. Photonics* **2013**, *7* (11), 907–912.
- (8) Ferrari, L.; Wu, C.; Lepage, D.; Zhang, X.; Liu, Z. Hyperbolic Metamaterials and Their Applications. *Prog. Quantum Electron.* **2015**, 40 (2014), 1–40.
- (9) Starko-Bowes, R.; Atkinson, J.; Newman, W.; Hu, H.; Kallos, T.; Palikaras, G.; Fedosejevs, R.; Pramanik, S.; Jacob, Z. Optical Characterization of Epsilon-near-Zero, Epsilon-near-Pole, and Hyperbolic Response in Nanowire Metamaterials. J. Opt. Soc. Am. B 2015, 32 (10), 2074–2080.
- (10) Noginov, M. A.; Barnakov, Y. A.; Zhu, G.; Tumkur, T.; Li, H.; Narimanov, E. E. Bulk Photonic Metamaterial with Hyperbolic Dispersion. *Appl. Phys. Lett.* **2009**, *94* (15), 151105.
- (11) Chandrasekar, R.; Wang, Z.; Meng, X.; Lagutchev, A.; Kim, Y. L.; Wei, A.; Boltasseva, A.; Shalaev, V. M. Lasing Action in Gold Nanorod Hyperbolic Metamaterials. *ACS Photonics* **2016**, *4* (3), 674–690
- (12) Yao, J.; Wang, Y.; Tsai, K. T.; Liu, Z.; Yin, X.; Bartal, G.; Stacy, A. M.; Wang, Y. L.; Zhang, X. Design, Fabrication and Characterization of Indefinite Metamaterials of Nanowires. *Philos. Trans. R. Soc., A* **2011**, 369 (1950), 3434–3446.
- (13) Zhang, X.; Liu, Z. Superlenses to Overcome the Diffraction Limit. *Nat. Mater.* **2008**, 7 (6), 435–441.
- (14) Poddubny, A.; Iorsh, I.; Belov, P.; Kivshar, Y. Hyperbolic Metamaterials. *Nat. Photonics* **2013**, *7* (12), 948–957.
- (15) Wang, M.; Ye, M.; Iocozzia, J.; Lin, C.; Lin, Z. Plasmon-Mediated Solar Energy Conversion via Photocatalysis in Noble Metal/Semiconductor Composites. *Adv. Sci.* **2016**, 3 (6), 1–14.
- (16) Gu, M.; Ouyang, Z.; Jia, B.; Stokes, N.; Chen, X.; Fahim, N.; Li, X.; Ventura, M. J.; Shi, Z. Nanoplasmonics: A Frontier of Photovoltaic Solar Cells. *Nanophotonics* **2012**, *1* (3–4), 235–248.
- (17) Joy, N. A.; Nandasiri, M. I.; Rogers, P. H.; Jiang, W.; Varga, T.; Kuchibhatla, S. V. N. T.; Thevuthasan, S.; Carpenter, M. A. Selective Plasmonic Gas Sensing: H 2, NO 2, and CO Spectral Discrimination by a Single Au-CeO 2 Nanocomposite Film. *Anal. Chem.* **2012**, *84* (11), 5025–5034.
- (18) Lu, L.; Simpson, R. E.; Valiyaveedu, S. K. Active Hyperbolic Metamaterials: Progress, Materials and Design. J. Opt. (Bristol, U. K.) 2018, 20 (10), 103001.
- (19) Li, L.; Sun, L.; Gomez-Diaz, J. S.; Hogan, N. L.; Lu, P.; Khatkhatay, F.; Zhang, W.; Jian, J.; Huang, J.; Su, Q.; et al. Self-Assembled Epitaxial Au-Oxide Vertically Aligned Nanocomposites for Nanoscale Metamaterials. *Nano Lett.* **2016**, *16* (6), 3936–3943.
- (20) Misra, S.; Li, L.; Zhang, D.; Jian, J.; Qi, Z.; Fan, M.; Chen, H. T.; Zhang, X.; Wang, H. Self-Assembled Ordered Three-Phase Au–BaTiO 3 ZnO Vertically Aligned Nanocomposites Achieved by a Templating Method. *Adv. Mater.* **2019**, *31* (7), 1806529.
- (21) Misra, S.; Li, L.; Jian, J.; Huang, J.; Wang, X.; Zemlyanov, D.; Jang, J.; Ribeiro, F. H.; Wang, H. Tailorable Au Nanoparticles Embedded in Epitaxial TiO2 Thin Films for Tunable Optical Properties. ACS Appl. Mater. Interfaces 2018, 10, 32895–32902.
- (22) Zhang, W.; Chen, A.; Bi, Z.; Jia, Q.; Macmanus-driscoll, J. L.; Wang, H. Interfacial Coupling in Heteroepitaxial Vertically Aligned Nanocomposite Thin Films: From Lateral to Vertical Control. *Curr. Opin. Solid State Mater. Sci.* **2014**, *18* (1), 6–18.
- (23) Zhang, W.; Chen, A.; Jian, J.; Zhu, Y.; Chen, L.; Lu, P.; Jia, Q.; Macmanus-driscoll, J. L.; Zhang, X.; Wang, H. Strong Perpendicular Exchange Bias in Epitaxial La0.7Sr0.3MnO3:BiFeO3 Nanocomposite Films through Vertical Interfacial Coupling. *Nanoscale* **2015**, 7, 13808–13815.
- (24) Fan, M.; Wang, H.; Misra, S.; Zhang, B.; Qi, Z.; Sun, X.; Huang, J.; Wang, H. Microstructure, Magnetic, and Magnetoresistance Properties of La0.7Sr0.3MnO3:CuO Nanocomposite Thin Films. ACS Appl. Mater. Interfaces 2018, 10 (6), 5779–5784.
- (25) Gao, X.; Li, L.; Jian, J.; Wang, H.; Fan, M.; Huang, J.; Wang, X.; Wang, H. Vertically Aligned Nanocomposite BaTiO 3:YMnO 3 Thin

- Films with Room Temperature Multiferroic Properties toward Nanoscale Memory Devices. ACS Appl. Nano Mater. 2018, 1 (6), 2509–2514.
- (26) Huang, J.; MacManus-Driscoll, J. L.; Wang, H. New Epitaxy Paradigm in Epitaxial Self-Assembled Oxide Vertically Aligned Nanocomposite Thin Films. *J. Mater. Res.* **2017**, 32 (21), 4054–4066.
- (27) Sun, X.; Li, Q.; Huang, J.; Fan, M.; Rutherford, B. X.; Paldi, R. L.; Jian, J.; Zhang, X.; Wang, H. Strain-Driven Nanodumbbell Structure and Enhanced Physical Properties in Hybrid Vertically Aligned Nanocomposite Thin Films. *Appl. Mater. Today* **2019**, *16*, 204–212.
- (28) Sun, X.; Huang, J.; Jian, J.; Fan, M.; Wang, H.; Li, Q.; Mac Manus-Driscoll, J. L.; Lu, P.; Zhang, X.; Wang, H. Three-Dimensional Strain Engineering in Epitaxial Vertically Aligned Nanocomposite Thin Films with Tunable Magnetotransport Properties. *Mater. Horiz.* **2018**, *5* (3), 536–544.
- (29) Sun, X.; Li, Q.; Huang, J.; Jian, J.; Lu, P.; Zhang, X.; Macmanus-Driscoll, J. L.; Wang, H. Strain and Property Tuning of the 3D Framed Epitaxial Nanocomposite Thin Films via Interlayer Thickness Variation. *J. Appl. Phys.* **2019**, *125*, 082530.
- (30) Huang, J.; Li, L.; Lu, P.; Qi, Z.; Sun, X.; Zhang, X.; Wang, H. Self-Assembled Co-BaZrO3 Nanocomposite Thin Films with Ultra-Fine Vertically Aligned Co Nanopillars. *Nanoscale* **2017**, 9 (23), 7970–7976.
- (31) Kabashin, A. V.; Evans, P.; Pastkovsky, S.; Hendren, W.; Wurtz, G. A.; Atkinson, R.; Pollard, R.; Podolskiy, V. A.; Zayats, A. V. Plasmonic Nanorod Metamaterials for Biosensing. *Nat. Mater.* **2009**, 8 (11), 867–871.
- (32) Melosh, N. A.; Boukai, A.; Diana, F.; Gerardot, B.; Badolato, A.; Petroff, P. M.; Heath, J. R. Ultrahigh-Density Nanowire Lattices and Circuits. *Science (Washington, DC, U. S.)* **2003**, 300 (5616), 112–115.
- (33) Shukla, S.; Kim, K. T.; Baev, A.; Yoon, Y. K.; Litchinitser, N. M.; Prasad, P. N. Fabrication and Characterization of Gold-Polymer Nanocomposite Plasmonic Nanoarrays in a Porous Alumina Template. ACS Nano 2010, 4 (4), 2249–2255.
- (34) Stepniowski, W. J.; Salerno, M. Fabrication of Nanowires and Nanotubes by Anodic Alumina Template-Assisted Electrodeposition. In *Manufacturing Nanostructures*; 2014; pp 321–357.
- (35) Hornyak, G. L.; Patrissi, C. J.; Oberhauser, E. B.; Martin, C. R.; Valmalette, J. C.; Lemaire, L.; Dutta, J.; Hofmann, H. Effective Medium Theory Characterization of Au/Ag Nanoalloy-Porous Alumina Composites. *Nanostruct. Mater.* 1997, 9 (1–8), 571–574.
- (36) Knight, M. W.; King, N. S.; Liu, L.; Everitt, H. O.; Nordlander, P.; Halas, N. J. Aluminum for Plasmonics. *ACS Nano* **2014**, *8* (1), 834–840.
- (37) Chan, G. H.; Zhao, J.; Hicks, E. M.; Schatz, G. C.; Van Duyne, R. P. Plasmonic Properties of Copper Nanoparticles Fabricated by Nanosphere Lithography. *Nano Lett.* **2007**, *7* (7), 1947–1952.
- (38) Gao, C.; Hu, Y.; Wang, M.; Chi, M.; Yin, Y. Fully Alloyed Ag/Au Nanospheres: Combining the Plasmonic Property of Ag with the Stability of Au. J. Am. Chem. Soc. 2014, 136 (20), 7474–7479.
- (39) Alissawi, N.; Zaporojtchenko, V.; Strunskus, T.; Kocabas, I.; Chakravadhanula, V. S. K.; Kienle, L.; Garbe-Schönberg, D.; Faupel, F. Effect of Gold Alloying on Stability of Silver Nanoparticles and Control of Silver Ion Release from Vapor-Deposited Ag-Au/Polytetrafluoroethylene Nanocomposites. *Gold Bull.* **2013**, *46* (1), 3–11.
- (40) Bobb, D.; Zhu, G.; Mayy, M.; Gavrilenko, A. V.; Mead, P.; Gavrilenko, V. I.; Noginov, M. A. Engineering of Low-Loss Metal for Nanoplasmonic and Metamaterials Applications. *Appl. Phys. Lett.* **2009**, 95, 151102.
- (41) Boltasseva, A.; Atwater, H. A. Low-Loss Plasmonic Metamaterials. *Science (Washington, DC, U. S.)* **2011**, 331 (January), 290–292.
- (42) Fang, H.; Yang, J.; Wen, M.; Wu, Q. Nanoalloy Materials for Chemical Catalysis. *Adv. Mater.* **2018**, *30* (17), 1705698.
- (43) Muñoz-Flores, B. M.; Kharisov, B. I.; Jiménez-Pérez, V. M.; Elizondo Martínez, P.; López, S. T. Recent Advances in the Synthesis

- and Main Applications of Metallic Nanoalloys. *Ind. Eng. Chem. Res.* **2011**, *50* (13), *7705–7721*.
- (44) Lee, K. E.; Hesketh, A. V.; Kelly, T. L. Chemical Stability and Degradation Mechanisms of Triangular Ag, Ag@Au, and Au Nanoprisms. *Phys. Chem. Chem. Phys.* **2014**, *16* (24), 12407–12414.
- (45) Huang, J.; Jin, T.; Misra, S.; Wang, H.; Qi, Z.; Dai, Y.; Sun, X.; Li, L.; Okkema, J.; Chen, H.-T.; Lin, P.-T.; Zhang, X.; Wang, H. Tailorable Optical Response of Au-LiNbO 3 Hybrid Metamaterial Thin Films for Optical Waveguide Applications. *Adv. Opt. Mater.* **2018**, *6* (19), 1800510.
- (46) Ferrando, R.; Jellinek, J.; Johnston, R. L. Nanoalloys: From Theory to Applications of Alloy Clusters and Nanoparticles. *Chem. Rev.* **2008**, *108* (3), 845–910.
- (47) Wu, Y.; Zhang, C.; Estakhri, N. M.; Zhao, Y.; Kim, J.; Zhang, M.; Liu, X. X.; Pribil, G. K.; Alù, A.; Shih, C. K.; et al. Intrinsic Optical Properties and Enhanced Plasmonic Response of Epitaxial Silver. *Adv. Mater.* **2014**, *26* (35), 6106–6110.
- (48) Chen, X.; Wu, Z.; Liu, D.; Gao, Z. Preparation of ZnO Photocatalyst for the Efficient and Rapid Photocatalytic Degradation of Azo Dyes. *Nanoscale Res. Lett.* **2017**, *12* (1), 4–13.
- (49) Vittal, R.; Ho, K. C. Zinc Oxide Based Dye-Sensitized Solar Cells: A Review. *Renewable Sustainable Energy Rev.* **2017**, 70 (March 2016), 920–935.
- (50) Rice, S. B.; Chan, C.; Brown, S. C.; Eschbach, P.; Han, L.; Ensor, D. S.; Stefaniak, A. B.; Bonevich, J.; Vladár, A. E.; Walker, A. R. H.; et al. Particle Size Distributions by Transmission Electron Microscopy: An Interlaboratory Comparison Case Study. *Metrologia* **2013**, *50* (6), 663–678.
- (51) Wang, X.; Jian, J.; Zhou, Z.; Fan, C.; Dai, Y.; Li, L.; Huang, J.; Sun, J.; Donohue, A.; Bermel, P.; Zhang, X.; Chen, H.-T.; Wang, H.; et al. Self-Assembled Ag—TiN Hybrid Plasmonic Metamaterial: Tailorable Tilted Nanopillar and Optical Properties. *Adv. Opt. Mater.* **2019**, *7* (3), 1801180.
- (52) Lee, K. S.; El-Sayed, M. A. Gold and Silver Nanoparticles in Sensing and Imaging: Sensitivity of Plasmon Response to Size, Shape, and Metal Composition. *J. Phys. Chem. B* **2006**, *110* (39), 19220–19225
- (53) Mubeen, S.; Lee, J.; Lee, W. R.; Singh, N.; Stucky, G. D.; Moskovits, M. On the Plasmonic Photovoltaic. *ACS Nano* **2014**, 8 (6), 6066–6073.
- (54) Xiang, X.; Yang, C.; Zhang, Y.; Peng, Z.; Cao, Z.; Zhao, H.; Zhang, P.; Xuan, L. Experimental Realization of Hyperbolic Dispersion Metamaterial for the Whole Visible Spectrum Based on Liquid Crystalline Phase Soft Template. *Opt. Express* **2015**, 23 (16), 21343–21351.
- (55) Baqir, M. A.; Choudhury, P. K.; Mughal, M. J. Gold Nanowires-Based Hyperbolic Metamaterial Multiband Absorber Operating in the Visible and Near-Infrared Regimes. *Plasmonics* **2019**, *14* (2), 485–492.
- (56) Reshetnyak, V. Y.; Pinkevych, I. P.; Urbas, A. M.; Evans, D. R. Controlling Hyperbolic Metamaterials with a Core-Shell Nanowire Array [Invited]. *Opt. Mater. Express* **2017**, *7* (2), 542.
- (57) Zong, R. L.; Zhou, J.; Li, Q.; Du, B.; Li, B.; Fu, M.; Qi, X. W.; Li, L. T.; Buddhudu, S. Synthesis and Optical Properties of Silver Nanowire Arrays Embedded in Anodic Alumina Membrane. *J. Phys. Chem. B* **2004**, *108* (43), 16713–16716.
- (58) Starko-Bowes, R.; Atkinson, J.; Newman, W.; Hu, H.; Kallos, T.; Palikaras, G.; Fedosejevs, R.; Pramanik, S.; Jacob, Z. Optical Characterization of Epsilon Near Zero, Epsilon Near Pole and Hyperbolic Reponse in Nanowire Metamaterials. *J. Opt. Soc. Am. B* **2015**, 32 (10), 2074–2080.